Rapid Protoplanet Formation in Vortices: Three-dimensional Local Simulations with Self-gravity

Wladimir Lyra[1] , Chao-Chin Yang (楊朝欽)[2] , Jacob B. Simon[3] , Orkan M. Umurhan[4,5] , and Andrew N. Youdin[6,7]

[1] New Mexico State University, Department of Astronomy, PO Box 30001 MSC 4500, Las Cruces, NM 88001, USA; wlyra@nmsu.edu
[2] Department of Physics and Astronomy, The University of Alabama, Box 870324, Tuscaloosa, AL 35487-0324, USA
[3] Department of Physics and Astronomy, Iowa State University, Ames, IA 50010, USA
[4] NASA Ames Research Center, Space Sciences Division, Planetary Sciences Branch, Moffatt Field, CA 94035, USA
[5] SETI, Carl Sagan Center, 190 Bernardo Way, Mountain View, CA 94043, USA
[6] Department of Astronomy and Steward Observatory, University of Arizona, Tucson, AZ 85721, USA
[7] The Lunar and Planetary Laboratory, University of Arizona, Tucson, AZ 85721, USA

Abstract

Disk vortices, seen in numerical simulations of protoplanetary disks and found observationally in Atacama Large Millimeter/submillimeter Array and Very Large Array images of these objects, are promising sites for planet formation given their pebble trapping abilities. Previous works have shown a strong concentration of pebbles in vortices, but gravitational collapse has only been shown in low-resolution, two-dimensional, global models. In this Letter, we aim to study the pebble concentration and gravitational collapse of pebble clouds in vortices via high-resolution, three-dimensional, local models. We performed simulations of the dynamics of gas and solids in a local shearing box where the gas is subject to convective overstability, generating a persistent giant vortex. We find that the vortex produces objects of Moon and Mars mass, with a mass function of power-law $d \ln N/d \ln M = -1.6 \pm 0.3$. The protoplanets grow rapidly, doubling in mass in about five orbits, following pebble accretion rates. The mass range and mass doubling rate are in broad agreement with previous low-resolution global models. We conclude that Mars-mass planetary embryos are the natural outcome of planet formation inside the disk vortices seen in millimeter and radio images of protoplanetary disks.

Unified Astronomy Thesaurus concepts: Planet formation (1241)

1. Introduction

Anticyclonic vortices in circumstellar disks have long been heralded as promising sites for planet formation, ever since they were independently suggested as such by Barge & Sommeria (1995), Adams & Watkins (1995), and Tanga et al. (1996). While cyclones are low pressure regions, in a disk the Keplerian shear ensures that only anticyclones survive. These anticyclones are pressure maxima, making them natural traps of dust pebbles (Klahr & Henning 1997; Bracco et al. 1999; Chavanis 2000). A gas parcel in a vortex is in geostrophic equilibrium between the negative pressure gradient, the Coriolis force, and the centrifugal force. In essence, the vortex behaves like a miniature disk, with the Coriolis force playing the role that stellar gravity does in the larger circumstellar disk. The pebble dynamics are likewise analogous. Once inside the vortex, a pebble orbits the vortex center due to the Coriolis force; yet, the pebble continuously loses angular momentum due to the drag force. As a result, pebbles drift steadily toward the center of the vortex, where they accumulate.

It was shown by Lyra et al. (2008a, 2009a, 2009b) that in the limit where turbulence in the vortex core is absent, the concentration of pebbles easily reaches the conditions necessary to gravitationally collapse them into planets. These simulations, albeit two-dimensional, show that disk vortices trap an ensemble of pebbles of total mass around the mass of Mars. Meheut et al. (2012) independently find similar results

with three-dimensional simulations. These results, however, were obtained with global simulations and thus of low resolution in the region of interest; most importantly, the turbulence in the vortex core could not be realized. Fluids in uniform rotation support a spectrum of stable inertial waves (see Chandrasekhar 1961). Strain is introduced when the motion passes from circular to elliptical, and some three-dimensional modes find resonance with the underlying strain field. The resulting elliptical instability (Bayly 1986; Pierrehumbert 1986; Kerswell 2002; Lesur & Papaloizou 2009) easily breaks the coherence of the vortex, feeding on its kinetic energy, which then cascades and dissipates. If vorticity is supplied in the integral scale, so that a steady state of "elliptic turbulence" is achieved, the vortex core develops rms velocities in the range 5%–10% of the sound speed (Lesur & Papaloizou 2010; Lyra & Klahr 2011).

The impact of this vortex core turbulence in pebble dynamics was worked out analytically by Klahr & Henning (1997) and Lyra & Lin (2013), showing that a steady state is reached where the inward drift of pebbles is balanced by turbulent diffusion. Simulations by Lyra et al. (2018) and Raettig et al. (2021) detail how this turbulent diffusion happens hydrodynamically, showing that the pebbles disrupt the vortex around the midplane but that the coherence of the three-dimensional vortex column is maintained.

These advances in the understanding of vortices in the past decade still left unanswered what the mass distribution of planets formed in vortices is, a quantity (the mass function) that has been measured in streaming instability calculations (though for much smaller mass objects; e.g., Johansen et al. 2015; Simon et al. 2016; Schäfer et al. 2017; Li et al. 2019; Gole et al. 2020). High

concentrations of pebbles with a dust-to-gas ratio above unity were observed in the simulations of Raettig et al. (2021), supporting the notion that the formation of planetary bodies was a likely outcome of the trapping. Indeed, some of the enhancements were above Hill density and would have collapsed gravitationally had self-gravity been included. Here we use the same model as Raettig et al. (2021), now including self-gravity, to determine the mass distribution of protoplanets formed in baroclinic vortices.

This Letter is structured as follows. We introduce the equations of motion in Section 2, followed by the results in Section 3. We conclude the Letter with a discussion of the results in Section 4.

2. Model

We use a baroclinic shearing box with the pressure gradient linearized, and an optically thin cooling law. The gas model is identical to the one used in Lyra & Klahr (2011), Lyra (2014), Raettig et al. (2013, 2015), Lyra et al. (2018), and Raettig et al. (2021), except that here we also include self-gravity of the particles. We solve the Poisson equation,

$$\nabla^2 \Phi = 4\pi G \rho_d, \quad (1)$$

via fast Fourier transforms, as in Johansen et al. (2007). Here Φ is the self-gravitational potential, ρ_d is the dust density, and G is the gravitational constant. The strength of self-gravity is set by the dimensionless parameter

$$\tilde{G} = \frac{4\pi G \rho_0}{\Omega^2}, \quad (2)$$

where ρ_0 is the reference density and Ω is the Keplerian frequency. The parameter $\tilde{G}$ is related to the Toomre Q parameter (for the gas) by $Q = \tilde{G}^{-1}\sqrt{8/\pi}$.

As particles concentrate, a gravitationally bound clump is replaced by a sink particle when the particle density increases above the Hill density (Johansen et al. 2015),

$$\rho_R \equiv \frac{9\Omega^2}{4\pi G}, \quad (3)$$

meaning that self-gravity overcomes tidal forces. This criterion does not include the effect of diffusion, which increases the density needed to collapse (Klahr & Schreiber 2020, 2021). As the simulation progresses, sink particles are free to grow in mass by accreting pebbles and other protoplanets.

We quote the masses in units of the Toomre mass (e.g., Abod et al. 2019; Li et al. 2019), which is the mass enclosed in a circular area of diameter equal to the Toomre wavelength λ_G and column density of pebbles Σ_p,

$$M_G = \pi\left(\frac{\lambda_G}{2}\right)^2 \Sigma_p, \quad (4)$$

where the Toomre wavelength is

$$\lambda_G = \frac{4\pi^2 G \Sigma}{\Omega^2}, \quad (5)$$

and Σ is the gas column density.

The box length is $4H \times 16H \times 2H$, where $H \equiv c_{s0}/\Omega$ is the scale height, and c_{s0} is the reference sound speed. The box is vertically unstratified, with periodic boundary conditions in y and z, and shear-periodic in x. The simulations were done with

the PENCIL CODE (Brandenburg & Dobler 2002, 2010; Pencil Code Collaboration et al. 2021) and carried out at multiple resolutions, as described in more detail below.

The global dust-to-gas ratio is set to 3×10^{-2}, and the Stokes number is 0.3, well in the regime of strong clumping (Carrera et al. 2015; Yang et al. 2017; Li & Youdin 2021), though we do not expect streaming instability, given our resolution. We use code units such that

$$c_p = \Omega = \rho_0 = 1. \quad (6)$$

Here c_p is the heat capacity at constant pressure, and ρ_0 is the reference volume density. Other parameters are the adiabatic index $\gamma = 1.4$, and $\tilde{G} = 0.1$. This value of $\tilde{G}$ corresponds to $Q \approx 16$, so the gas self-gravity is negligible. We also define the aspect ratio $h \equiv H/r = 0.1$ and finally, we set $\Pi \equiv \Delta v/c_{s0} = 0.125$, where Δv is the velocity reduction on the gas, with respect to Keplerian, due to the global pressure gradient. This value is justified given $\Delta v = v_K \mathcal{O}(h^2)$, i.e., the Keplerian velocity v_k scaled by a factor of second order in aspect ratio, so the value of Π is of first order in aspect ratio, i.e., $\Pi = \mathcal{O}(h)$.

Conversion from code units to physical units necessitates choosing a box location and stellar mass, which sets the physical value of Ω. For a box orbiting a solar mass at 20 au, the reference volume density at the midplane is then given by Equation (2), yielding $\rho_g \approx 6 \times 10^{-13}\,\mathrm{g\,cm^{-3}}$. The column density is $\Sigma \approx 44\,\mathrm{g\,cm^{-2}}$. The box has 12.75 Earth masses of dust. The Toomre mass is $M_G \approx 8.7 \times 10^{-5}M_\oplus$. Assuming $\rho_\bullet = 3\,\mathrm{g\,cm^{-3}}$ for the grains, the Stokes number St = 0.3 implies grain radius $a_\bullet = 1.7$ cm.

The gas model is identical to Lyra (2014), Lyra et al. (2018), and Raettig et al. (2021), and the reader is referred to these papers for an exhaustive description. For the fiducial model we use resolution 256^3 (we also ran 128^3 and 512^3). The cells are noncubic; the equal number of cells in different directions is needed for the Poisson solver. The box is seeded with Gaussian noise in the velocity at the $10^{-3}c_s$ level. The cooling time is $\tau = \gamma^{-1}$, to maximize the growth rate of the convective overstability (Klahr & Hubbard 2014; Lyra 2014; Latter 2016; Teed & Latter 2021). The simulation is run for 400 orbits until the convective overstability saturates and a single large vortex dominates the box. We emphasize that these thermodynamical conditions are unrealistic, but our goal in using the convective overstability is simply to produce a vortex in a robust and generic way. More realistic thermodynamics would simply slow down the evolution to a similar saturated state.

After the vortex saturates, 7.5×10^6 superparticles are introduced. A superparticle represents a swarm of pebbles sharing the same position, velocity, and aerodynamical properties. At this resolution, the mass of an individual superparticle is 10^{22} g (10^{-4} lunar masses, or 10^{-2} Ceres mass).

3. Results

Figure 1 overplots the gravitationally bound objects formed (black and white symbols) against the z-averaged gas vertical vorticity (left panel) and the pebble column density (right panels). The upper plots are from a snapshot at 2 orbits after inclusion of particles, the middle one at 5, and the lower at 12 orbits. We see at two orbits that indeed the formation of the gravitationally bound clumps happens inside the vortex. The vortex is colocated with an extended region of high pebble density, which spawns the clumps. The middle panel shows
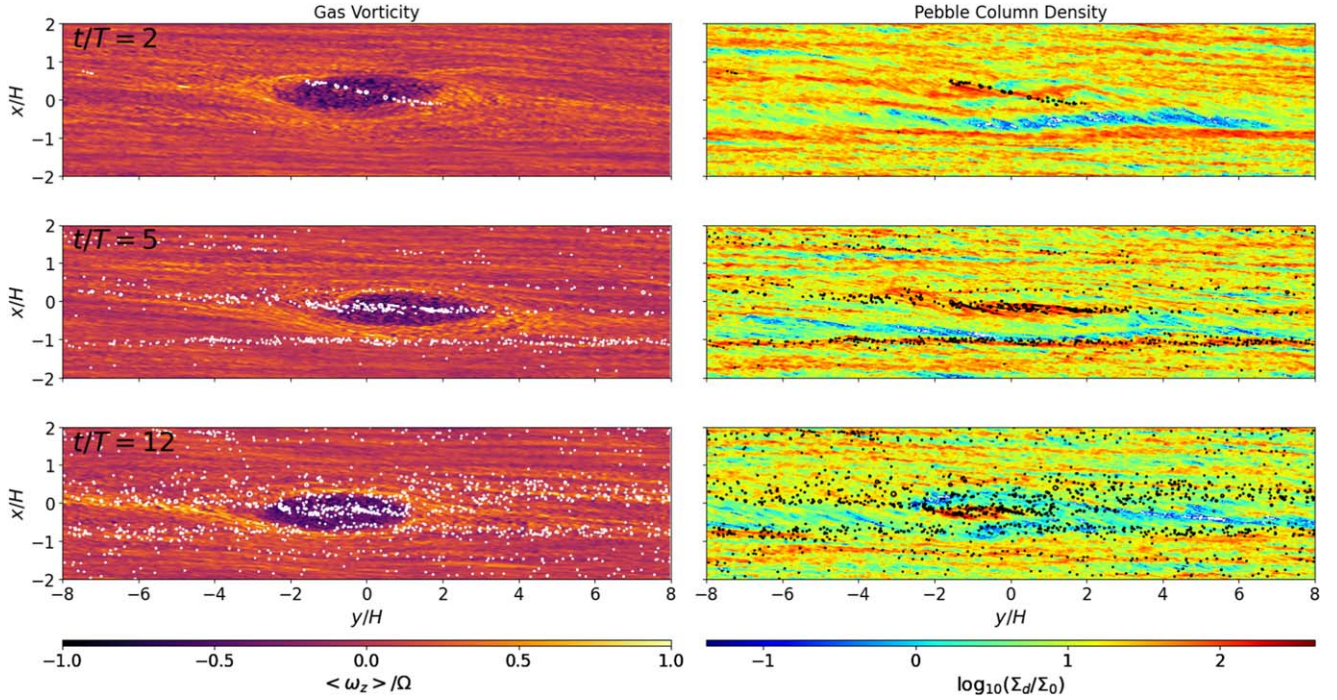
Figure 1. Distribution of protoplanets formed in the higher resolution model (512^3 mesh resolution, 7.5×10^6 superparticles). The left panels show the vertically averaged vertical vorticity; the right panels show the vertically integrated (column) density of pebbles. The upper panels correspond to 2 orbits after the insertion of particles, the middle panel after 5, and the lower panel after 12 orbits. The protoplanets are overlaid as white circles in the left panels, and black circles in the right panels. The radius of the circle marks the Hill radius of the protoplanet. Protoplanets are formed inside the vortex, which continuously spawns planetary mass objects.
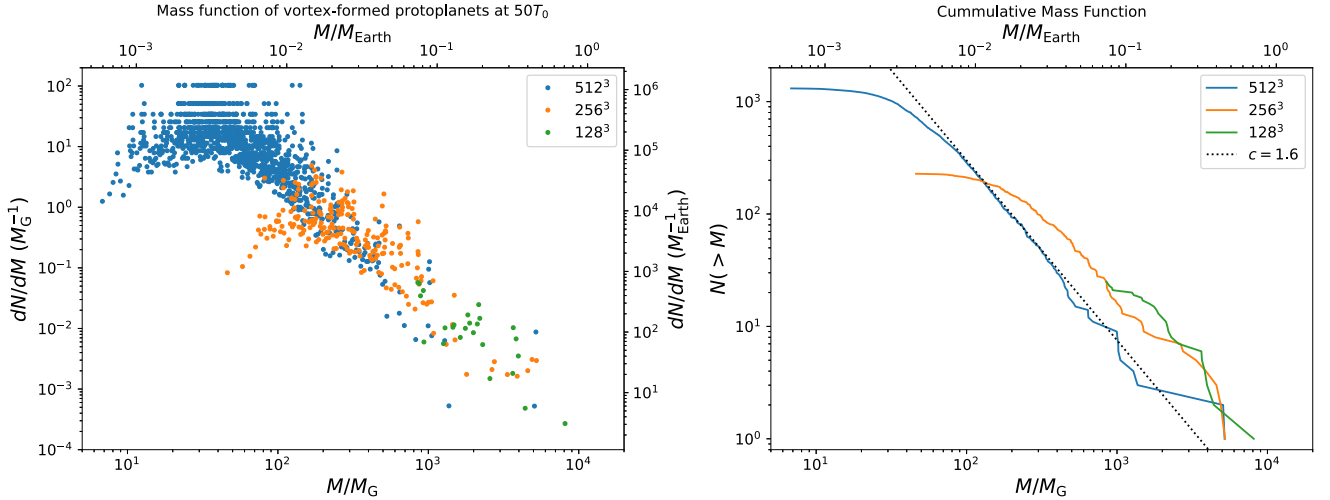
Figure 2. Left: differential mass function, 50 orbits after particle insertion, as a function of resolution. The simulations converge at high mass, but as we increase the resolution, more small mass objects are formed, with no convergence in sight. The horizontal stripes seen from our highest 512^3 resolution is due to the mass discretization of the superparticles; see Equation (7). Right: cumulative mass function, 50 orbits after particle insertion, as a function of resolution.

that the objects do not stay in the vortex because, unlike the pebbles, they do not feel the gas drag. The vortex indeed functions as a "planet formation factory," turning pebbles into planets, that then leave the vortex, which, in turn, forms more planets. A ridge of high pebble density, colocated with bound objects, is seen at $x \approx -0.1H$. The lower panel shows the spatial distribution of the protoplanets at 12 orbits.

3.1. The Vortex Spawns Protoplanets

The typical mass of the objects formed is between the mass of the Moon and Mars, making them not planetesimals, but protoplanets. At two orbits in 256^3 resolution, eight protoplanets

are already formed, the smallest mass at 0.4 lunar masses, and the biggest at 5 lunar masses. Given the particle resolution (10^{22} g), these masses are resolved, particle-wise. At the grid level, though, the mass at the time of collapse is close to the Hill density. A cell volume at 256^3 resolution is $\Delta x \Delta y \Delta z = 2 \times 10^{35}$ cm^3. The Hill density ($\approx 5 \times 10^{-11}$) filling this cell corresponds to a mass of 10^{25} g, or 0.15 lunar mass, close to the lowest mass formed.

We run a resolution study to check if the initial mass function changes with grid resolution. Figure 2 shows the mass functions, differential (left panel) and cumulative (right panel) for different resolutions, 128^3, 256^3, and 512^3, taken at 50 orbits after particle
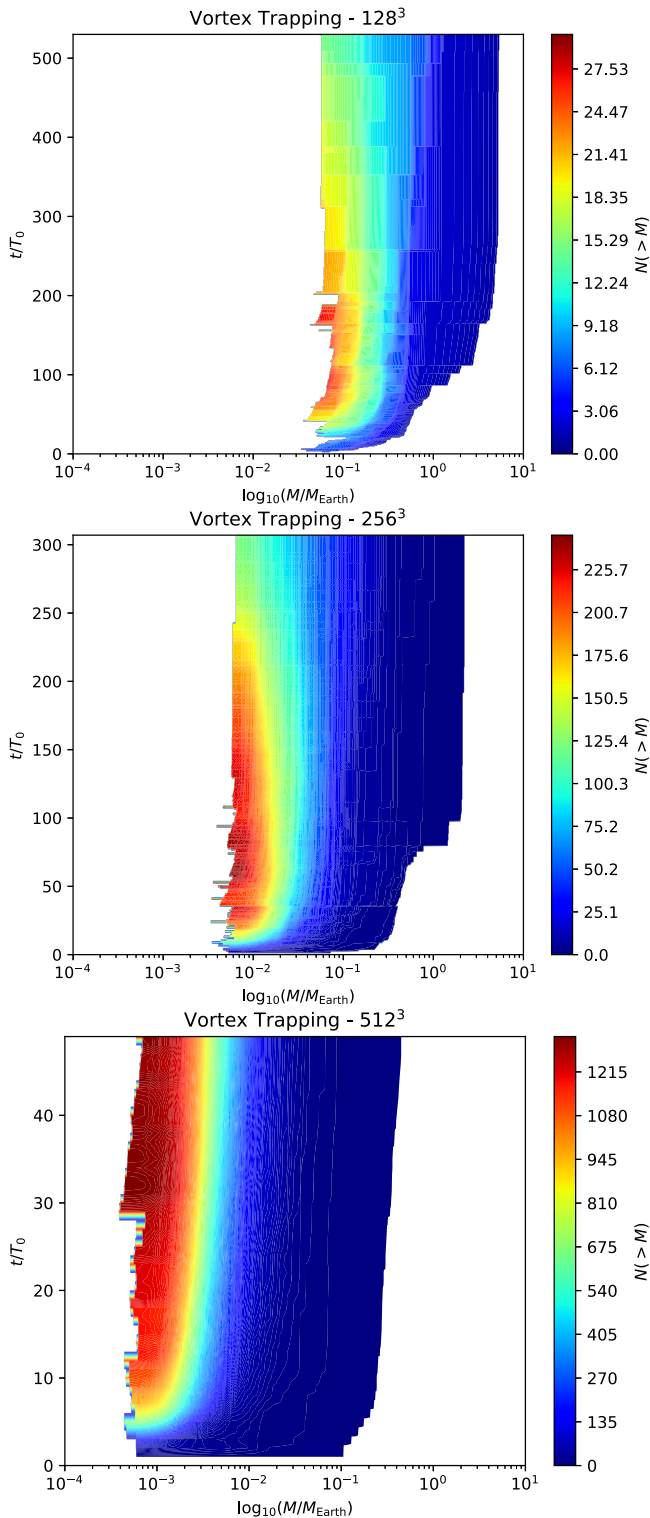
Figure 3. Evolution of the cummulative mass distribution, as a function of resolution. Notice the different final times. The mass distribution did not converge in time or resolution.
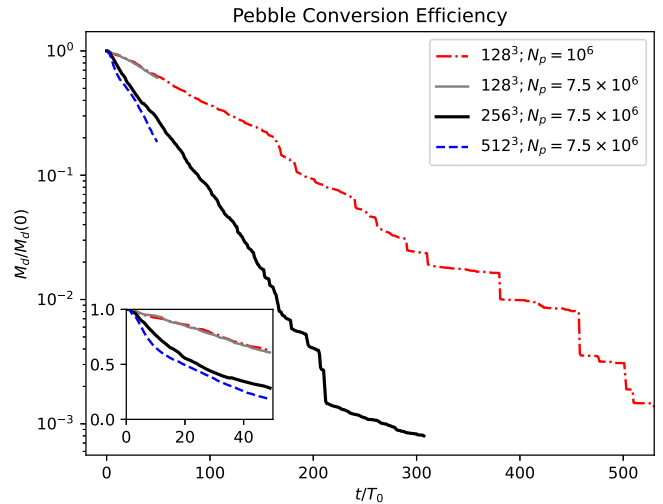

Figure 4. Efficiency of conversion of pebbles into protoplanets. The y-axis in the inset is shown in linear scale. Seen from the 128^3 at different particle resolution, that quantity has converged. Convergence is not seen with mesh resolution, although 256^3 to 512^3 has not changed the rate as much as from 128^3 to 256^3. At 256^3 resolution the available dust density drops 1 order of magnitude in 100 orbits.

objects, where $i-1$ and $i+1$ do not exist, respectively, in which case the first-order accurate forward and backward derivative is used, respectively.

As resolution increases, more protoplanets of low mass are formed, the lowest being $5 \times 10^{-4} M_\oplus$ (≈ 3 Ceres masses), with no convergence seen at low masses as we increase the resolution. The cumulative mass function shows that a power law of -1.6 follows in the resolved domain, flattening toward the bottom quarter of the logarithmic domain in mass.

In Figure 3 we plot the time evolution of the cumulative mass distribution, to check for convergence in time, i.e., if the distribution has reached a steady state. Snapshots at every orbit are taken, and the mass function (which is continuous) is interpolated to a range from 10^{-4} to $10 M_\oplus$, with 1000 points, log-spaced. We see that after planet formation starts, the number of objects in all mass bins increases steadily. The formation of lower-mass objects at increasing resolution is also clear. Some pixelization at low and high masses is seen as a result of the interpolation procedure. At later times, seen in the 128^3 and 256^3 runs (notice the different final times), growth stalls at the high-mass end. The timescale of the hydrodynamical simulation does not allow for convergence in the high-mass end, as binary collisions become the main driver of mass growth, which happen at much longer timescales (Sándor et al. 2011).

To check for particle resolution, we run a simulation with only 10^6 particles at 128^3 resolution, to compare with the "fiducial" particle resolution of 7.5×10^6. Figure 4 shows that the efficiency of pebble conversion is converged for particle resolution, depending instead on the resolution of the mesh. For the 256^3 model, at the end of the simulation, only 5998 of the original 7.5×10^6 superparticles remain, that is, 99.9% of the pebbles have been converted into protoplanets. The number was 99.6% at 200 orbits, 92% at 100 orbits, and 72% at 50 orbits.

3.2. Varying Stokes Number and Dust-to-gas Ratio

Figure 5 tracks the density of pebbles in a series of simulations. The fiducial model is the gray curve (resolution 256^3, $Z = 10^{-2}$, and $St = 0.3$). The pebble density steadily
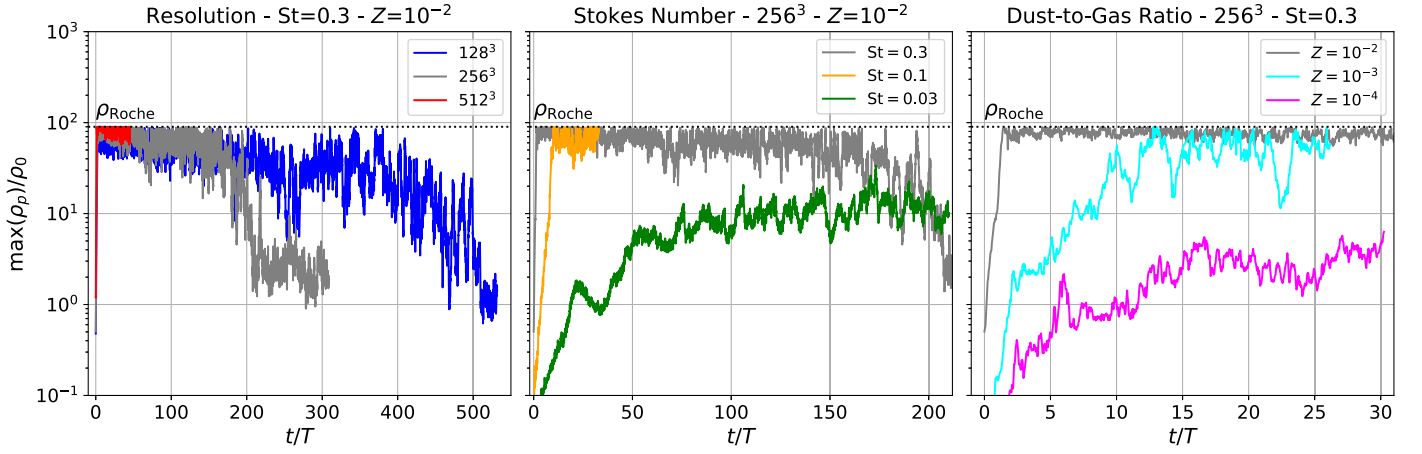
insertion. The differential mass function is calculated as

$$\left.\frac{dN}{dM}\right|_i = \frac{2}{M_{i+1} - M_{i-1}}, \qquad (7)$$

i.e., the second-order accurate centered first derivative. This form is used except for the least massive and most massive

Figure 5. Time evolution of the maximum pebble density as a function of resolution (left), Stokes number (middle), and dust-to-gas ratio (right). The Hill density for this simulation is $\rho_d = 90$ in code units. When a clump of pebbles achieves this density, a sink particle replaces it.
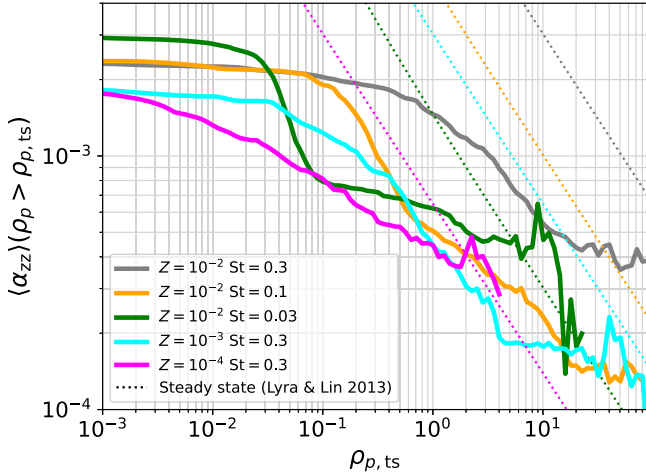

Figure 6. Density-diffusion relation for the 256^3 resolution runs shown in Figure 5. The *x*-axis shows a pebble density threshold, and the *y*-axis the diffusion computed as an average of all mesh cells with pebble density above the threshold, in space and time (see the main text). The dotted lines show the steady-state solution of Lyra & Lin (2013) for pebbles trapped in a vortex considering stellar vertical gravity, drag force, and diffusion. The runs that achieve collapse (Hill density $\rho_p = 90$) have diffusion under the steady-state prediction. The runs that do not achieve collapse (green line and magenta line) have maximum density consistent with the analytical solution.

increases to the Hill density (≈ 90 in code units) within less than two orbits after the inclusion of pebbles, forming the first protoplanets. As a gravitationally bound clump is replaced by a sink particle and the pebbles of the clump are removed from the simulation, the maximum pebble density stays constant after reaching Hill density. Protoplanet formation stops after ≈ 150 orbits, after which time the maximum density drops below the Hill density for the remainder of the simulation (until 300 orbits). In the 128^3 simulation (blue curve in left plot), planet formation continues intermittently until about 400 orbits. The middle panel shows the fiducial simulation and those of different Stokes numbers. For $St = 0.1$, planet formation is barely delayed, from 2 to 10 orbits. For $St = 0.03$, however, even after 150 orbits the pebble concentration has not achieved gravitational collapse, with the maximum pebble density reaching a plateau at about 10.

The right panel shows the dependency on the initial dust-to-gas ratio. At $Z = 10^{-3}$, planet formation happens nearly as fast as in the prior $St = 0.1$ case at $Z = 10^{-2}$. At $Z = 10^{-4}$, the

simulation did not lead to gravitational collapse, although the dust-to-gas ratio did rise above unity, stabilizing around 3.

To understand why some simulations lead to gravitational collapse and some do not, we consider the analytical solution of Lyra & Lin (2013). If the pebbles are trapped in a Kida vortex (Kida 1981) in a steady state between diffusion, drag force, and stellar vertical gravity then the peak pebble density is

$$\frac{\max(\rho_p)}{\rho_0} = Z\left(\frac{St}{\delta} + 1\right)^{1.5}, \tag{8}$$

where δ is the dimensionless diffusion coefficient, similar to the Shakura–Sunyaev α parameter (Shakura & Sunyaev 1973).

Figure 6 shows the diffusion versus ρ_p relation for these different runs. The *x*-axis is a dust density threshold, $\rho_{p,ts}$, and the *y*-axis is the diffusion parameter considering only the mesh cells that have dust density above this threshold. The diffusion is estimated as simply the vertical Mach number squared,

$$\alpha_{zz} \equiv \frac{u_z^2}{c_s^2}, \tag{9}$$

and the median is taken in both space (all cells above the threshold) and time. The time cadence is one orbit. For the $Z = 10^{-2}$ and $St = 0.3$ run (gray line), the time interval for averaging was 1 to 100 orbits; for the $Z = 10^{-2}$ and $St = 0.1$ run (orange line), 10 to 32 orbits; for the $Z = 10^{-2}$ and $St = 0.03$ (green line), 75 to 173 orbits; $Z = 10^{-3}$ and $St = 0.3$ (cyan line), 10 to 26, and finally for $Z = 10^{-4}$ and $St = 0.3$ (magenta line), 15 to 30 orbits. We overplot (dotted lines) the steady-state solution (Equation (8)) for the different combinations of parameters. We see that in the runs for which collapse occurs (ρ_p reaching 90) the diffusion is always under the steady-state prediction. For the $Z = 10^{-2}$ and $St = 0.3$ run, for instance, Hill density should be achieved for $\delta \sim \alpha_{zz}$ up to 7×10^{-4}, whereas the diffusion is about half this number. Conversely, the simulations that do not achieve collapse have maximum density consistent with the expected amount of diffusion measured. For $St = 0.03$ and $Z = 10^{-2}$, the prediction for $\rho_{p,max} \sim 10$ is $\delta = 3 \times 10^{-4}$. Indeed, that is approximately the α_{zz} measured (green line) for that density threshold. Similarly, for $St = 0.03$ and $Z = 10^{-2}$, the prediction for $\rho_{p,max} \sim 3$ is again $\delta = 3 \times 10^{-4}$, which too is measured (magenta line) for

that density threshold. This is an interesting agreement between the analytical prediction and the simulation, considering that the solution of Lyra & Lin (2013) does not consider the backreaction of the drag force, which becomes significant for dust-to-gas ratios near and above unity. Indeed, the fact that there is a decrease of the alpha value inside the vortex compared to the outside ($\rho_p \ll 1$) shows that the pebble concentration depresses the diffusion. That the steady-state solution holds at this regime shows that the vortex streamlines are not severely modified by the pebble concentration, as already shown by Lyra et al. (2018) and Raettig et al. (2021).

4. Conclusion

In this Letter, we investigate the formation of planetary-mass bodies in vortices (formed by convective overstability), including particle self-gravity. The inclusion of self-gravity allows us to follow the gravitational collapse of the particle clumps concentrated in the vortices. We model the gas for 400 orbits before the insertion of the particles to let the vortex develop. Our main result is that protoplanets of large size (of the order of the mass of Mars) are formed from the direct gravitational collapse of the pebble clouds, bypassing the planetesimal stage.

The same conclusion was found over a decade ago by Lyra et al. (2008b, 2009a, 2009b), albeit in two-dimensional models in low resolution. Here we show that those results were resolved in the high-mass end, and also not an artifact of the two-dimensionality. Even when we resolve smaller scales, we find that it is protoplanets that form, and not smaller planetesimals (although we could not find convergence with resolution, so planetesimals may form at the small mass end.). In our shearing box three-dimensional simulations, the vortex forms dozens of Mars-mass objects and hundreds of Moon-mass objects, in agreement with the previous simulations. The protoplanets rapidly grow, doubling in mass in about five orbits. The mass accretion rate is consistent with those found in Lyra et al. (2008a, 2009a), and in agreement with the mass accretion rate due to pebble accretion (Lambrechts & Johansen 2012), albeit with a much larger cross section (Cummins et al. 2022).

In our models, gravitationally bound clumps are replaced by sink particles, which are not affected by the drag force. All particles in the cell where the clump is located are converted into a sink. Unlike calculations where the drag force keeps influencing the gravitationally bound clump, we see that the protoplanets drift away from the vortex, which keeps producing planets.

We measure the mass function to be well-fit by a power-law $d \ln N / d \ln M = -1.6 \pm 0.3$ between lunar and Mars mass. Intriguingly, even though our model does not resolve the streaming instability, a power-law index of -1.6 was also found by Johansen et al. (2015; for sufficiently small masses in their mass function) and Simon et al. (2016) in streaming instability simulations. That different processes (streaming instability and vortex trapping) lead to the same slope for the mass function might suggest a universality in the outcome of planet formation, irrespective of the formation process. However, more recent works (e.g., Abod et al. 2019; Li et al. 2019; Gole et al. 2020) find slightly shallower power laws, when exponential truncation of the power law is used. In these works, such shallower power laws and an exponential

truncation were a better fit than the -1.6 slope. In our vortex models, we do not see a clear need for tapering, as opposed to the mass function of the streaming instability (e.g., Schäfer et al. 2017; Abod et al. 2019). The difference seen could also be due to resolution since we attained only $128/H$ in the highest resolution we ran, compared to $320/H$ in the lowest resolution modeled by Johansen et al. (2015) and Simon et al. (2016), and $2560/H$ in their highest. A model that resolves streaming instability and vortex trapping in the same simulation will be necessary to settle the question.

Gibbons et al. (2014, 2015) report relatively small objects (most massive bound clumps about 2-3 times smaller than the Moon) in 2D shearing sheet models of selfgravitating disks, likely due to different vortex dynamics in gravitational turbulence. In their case, the vortices are small (less than a scale height in radius) and intermittent (about 2 orbits). With smaller cross section for dust capture and less time to gather grains and collapse them, it is unsurprising that the protoplanets formed should be smaller.

Our results show that vortices are efficient formation sites of Mars-mass planetary embryos. In the present work, Pluto-mass objects are still formed via direct gravitational collapse. However, even the smallest objects formed are still about 10 times the Toomre mass. Clearly, the Toomre mass is not the characteristic mass of the problem (see also Abod et al. 2019). It remains to be explored whether streaming instability would operate inside a vortex, which could potentially lead to smaller masses at formation. This would necessitate even higher-resolution models, which we will explore in future work.

ORCID iDs

Wladimir Lyra ⬤ https://orcid.org/0000-0002-3768-7542
Chao-Chin Yang (楊朝欽) ⬤ https://orcid.org/0000-0003-2589-5034
Jacob B. Simon ⬤ https://orcid.org/0000-0002-3771-8054
Orkan M. Umurhan ⬤ https://orcid.org/0000-0001-5372-4254
Andrew N. Youdin ⬤ https://orcid.org/0000-0002-3644-8726

References

Abod, C. P., Simon, J. B., Li, R., et al. 2019, ApJ, 883, 192
Adams, F. C., & Watkins, R. 1995, ApJ, 451, 314
Astropy Collaboration, Robitaille, T. P., Tollerud, E. J., et al. 2013, A&A, 558, A33
Barge, P., & Sommeria, J. 1995, A&A, 295, L1
Bayly, B. J. 1986, PhRvL, 57, 2160
Bracco, A., Chavanis, P. H., Provenzale, A., & Spiegel, E. A. 1999, PhFl, 11, 2280
Brandenburg, A., & Dobler, W. 2002, CoPhC, 147, 471
Brandenburg, A., & Dobler, W. 2010, Pencil: Finite-difference Code for Compressible Hydrodynamic Flows, Astrophysics Source Code Library, ascl:1010.060
Carrera, D., Johansen, A., & Davies, M. B. 2015, A&A, 579, A43
Caswell, T. A., Droettboom, M., Lee, A., et al. 2020, matplotlib/matplotlib: REL: v3.3.3, Zenodo, doi:10.5281/zenodo.4268928
Chandrasekhar, S. 1961, Hydrodynamic and Hydromagnetic Stability (Oxford: Oxford University Press)
Chavanis, P. H. 2000, A&A, 356, 1089
Cummins, D. P., Owen, J. E., & Booth, R. A. 2022, MNRAS, 515, 1276
Gibbons, P. G., Mamatsashvili, G. R., & Rice, W. K. M. 2014, MNRAS, 442, 361
Gibbons, P. G., Mamatsashvili, G. R., & Rice, W. K. M. 2015, MNRAS, 453, 4232
Gole, D. A., Simon, J. B., Li, R., Youdin, A. N., & Armitage, P. J. 2020, ApJ, 904, 132
Harris, C. R., Millman, K. J., van der Walt, S. J., et al. 2020, Natur, 585, 357
Hunter, J. D. 2007, CSE, 9, 90
Johansen, A., Mac Low, M.-M., Lacerda, P., & Bizzarro, M. 2015, SciA, 1, 1500109
Johansen, A., Oishi, J. S., Mac Low, M.-M., et al. 2007, Natur, 448, 1022
Kerswell, R. R. 2002, AnRFM, 34, 83

Kida, S. 1981, JPSJ, 50, 3517
Klahr, H., & Hubberd, A. 2014, ApJ, 788, 21
Klahr, H., & Schreiber, A. 2020, ApJ, 901, 54
Klahr, H., & Schreiber, A. 2021, ApJ, 911, 9
Klahr, H. H., & Henning, T. 1997, Icar, 128, 213
Kluyver, T., Ragan-Kelley, B., Pérez, F., et al. 2016, in Positioning and Power in Academic Publishing: Players, Agents and Agendas, ed. F. Loizides & B. Scmidt (Amsterdam: IOS Press), 87
Lambrechts, M., & Johansen, A. 2012, A&A, 544, A32
Latter, H. N. 2016, MNRAS, 455, 2608
Lesur, G., & Papaloizou, J. C. B. 2009, A&A, 498, 1
Lesur, G., & Papaloizou, J. C. B. 2010, A&A, 513, A60
Li, R., & Youdin, A. N. 2021, ApJ, 919, 107
Li, R., Youdin, A. N., & Simon, J. B. 2019, ApJ, 885, 69
Lyra, W. 2014, ApJ, 789, 77
Lyra, W., Johansen, A., Klahr, H., & Piskunov, N. 2008a, A&A, 491, L41
Lyra, W., Johansen, A., Klahr, H., & Piskunov, N. 2008b, A&A, 479, 883
Lyra, W., Johansen, A., Klahr, H., & Piskunov, N. 2009a, A&A, 493, 1125
Lyra, W., Johansen, A., Zsom, A., Klahr, H., & Piskunov, N. 2009b, A&A, 497, 869
Lyra, W., & Klahr, H. 2011, A&A, 527, A138
Lyra, W., & Lin, M.-K. 2013, ApJ, 775, 17
Lyra, W., Raettig, N., & Klahr, H. 2018, RNAAS, 2, 195
Meheut, H., Keppens, R., Casse, F., & Benz, W. 2012, A&A, 542, A9
Meurer, A., Smith, C. P., Paprocki, M., et al. 2017, PeerJ Computer Science, 3, e103
Pencil Code Collaboration, Brandenburg, A., Johansen, A., et al. 2021, JOSS, 6, 2807
Perez, F., & Granger, B. E. 2007, CSE, 9, 21
Pierrehumbert, R. T. 1986, PhRvL, 57, 2157
Raettig, N., Klahr, H., & Lyra, W. 2015, ApJ, 804, 35
Raettig, N., Lyra, W., & Klahr, H. 2013, ApJ, 765, 115
Raettig, N., Lyra, W., & Klahr, H. 2021, ApJ, 913, 92
Sándor, Z., Lyra, W., & Dullemond, C. P. 2011, ApJL, 728, L9
Schäfer, U., Yang, C.-C., & Johansen, A. 2017, A&A, 597, A69
Shakura, N. I., & Sunyaev, R. A. 1973, A&A, 24, 337
Simon, J. B., Armitage, P. J., Li, R., & Youdin, A. N. 2016, ApJ, 822, 55
Tanga, P., Babiano, A., Dubrulle, B., & Provenzale, A. 1996, Icar, 121, 158
Teed, R. J., & Latter, H. N. 2021, MNRAS, 507, 5523
Trecakov, S., & Von Wolff, N. 2021, Practice and Experience in Advanced Research Computing, PEARC '21 (New York: Association for Computing Machinery)
Yang, C. C., Johansen, A., & Carrera, D. 2017, A&A, 606, A80